

High Thermoelectric Performance SnTe–In₂Te₃ Solid Solutions Enabled by Resonant Levels and Strong Vacancy Phonon Scattering

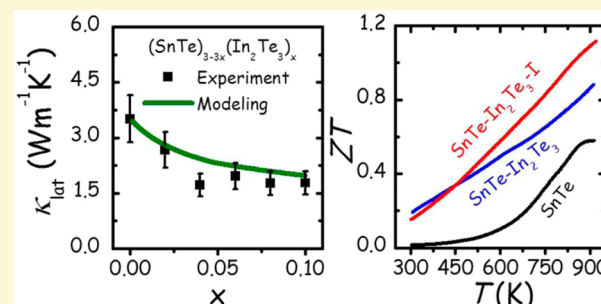
Gangjian Tan,[†] Wolfgang G. Zeier,[‡] Fengyuan Shi,[‡] Pengli Wang,[†] G. Jeffery Snyder,[‡] Vinayak P. Dravid,[‡] and Mercouri G. Kanatzidis*,^{†,‡,§}

[†]Department of Chemistry and [‡]Department of Materials Science and Engineering, Northwestern University, Evanston, Illinois 60208, United States

[§]Materials Science Division, Argonne National Laboratory, Argonne, Illinois 60439, United States

Supporting Information

ABSTRACT: Herein, we report a significantly improved thermoelectric figure of merit ZT of ~ 1.1 at ~ 923 K in p-type SnTe through In₂Te₃ alloying and iodine doping. We propose that the introduction of indium at Sn sites in SnTe creates resonant levels inside the valence bands, thereby considerably increasing the Seebeck coefficients and power factors in the low-to-middle temperature range. Unlike SnTe–InTe, the SnTe–In₂Te₃ system displays much lower lattice thermal conductivity. Utilizing a model for point defect scattering, we analyze the origin of the low thermal conductivity in SnTe–In₂Te₃ and attribute it mainly to the strong vacancy originated phonon scattering between Sn atoms and the vacancies introduced by In₂Te₃ alloying and partly to the interfacial scattering by In-rich nanoprecipitates present in SnTe matrix. By alloying only In₂Te₃ with SnTe, a ZT value of ~ 0.9 at 923 K was achieved. ZT can be further increased to ~ 1.1 at 923 K through adjusting the charge carriers by iodine doping at Te sites.



1. INTRODUCTION

Rock-salt structured SnTe has recently been recognized as a promising isomorphic alternative for PbTe in large-scale thermoelectric power generation application because it is more environmentally friendly.^{1–12} However, it is a great challenge to increase the performance of SnTe to the same level as PbTe.^{13–16} The reasons behind this are twofold: one, owing to its electronic structure, which governs the Seebeck coefficient, while the other due to its microstructure, which aids in phonon scattering. (1) As shown in Figure 1a,b, although both SnTe^{17–19} and PbTe^{20–22} feature two valence bands (one upper light-hole band at L point and one lower heavy-hole band at Σ point, separated by an energy gap of ΔE), the room-temperature ΔE in SnTe (~ 0.35 eV)^{17,19} is much larger than that in PbTe (~ 0.17 eV).^{20,21} Such a large ΔE in SnTe means that its Seebeck coefficient should be very low because the lower hole band with higher valley degeneracy is hard to be involved in electron transport under normal circumstances.¹¹ Indeed, with identical hole concentrations, the room-temperature Seebeck coefficient of SnTe is inferior to that of PbTe as indicated by the Pisarenko plot^{10,23} (Figure 1c). (2) The lattice thermal conductivity of SnTe is much higher than that of PbTe²⁴ because Sn is much lighter than Pb (Figure 1d). As a large Seebeck coefficient and low lattice thermal conductivity are crucial measures for a high figure of merit ZT , one needs to subtly tailor the electron and phonon transport of SnTe to achieve a comparable performance to PbTe.

Recent efforts to modify the valence band structure of SnTe with the aim to influence its Seebeck coefficient have been successful. Specifically that Cd, Hg, Mg, and Mn doping in SnTe could enhance the Seebeck coefficient of SnTe by means of pushing the two valence bands closer in energy, i.e., band convergence.^{2,5,7,25} An alternative way is to introduce additional impurity states (resonant levels) near the Fermi level by guest atom alloying, as implemented in p-type Tl-doped PbTe¹⁶ and In-doped SnTe^{10,26} and n-type Al-doped PbSe.²⁷ As effective as modifying the band structure is, in terms of improving the electronic transport properties, the phonon transport is unaltered or only mildly influenced via point defect scattering by these small impurities.^{2,5–7,10,11} This makes sense because the atomic mass and radius contrasts between Sn and the doping elements are usually fairly small, while strong point defect scattering of phonons usually requires a significant difference in atomic properties between the host and guest atoms.^{28–35}

The maximum mass contrast between the host and guest atom is maximum when $\Delta M/M = 1$ which appears unattainable by a conventional doping method, but is possible to achieve when the guest or host atom represents a vacancy. This reminds us of the partially filled skutterudites $F_yCo_4Sb_{12}$ (F and y stand for the filler atom and filling fraction, respectively; $y <$

Received: September 23, 2015

Revised: October 15, 2015

Published: November 6, 2015

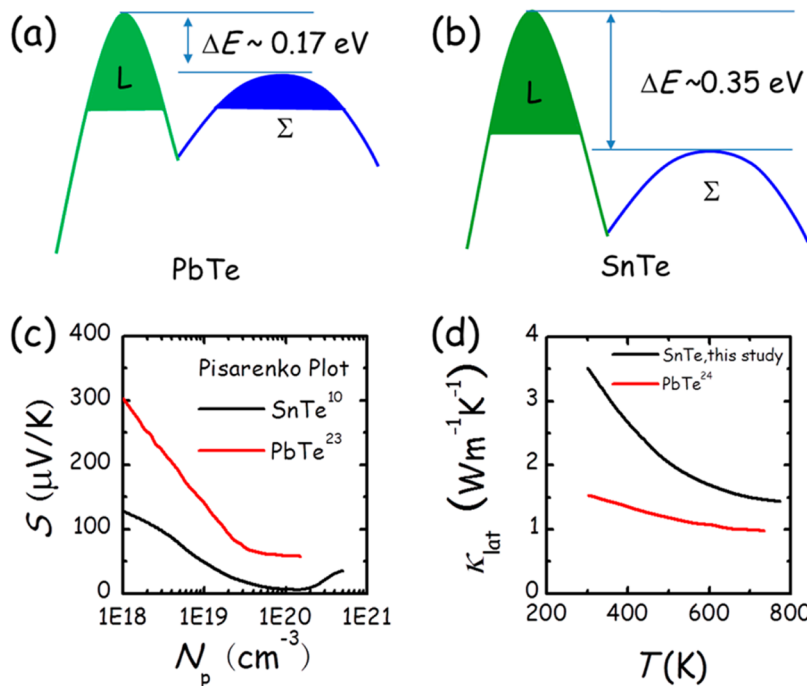


Figure 1. Schematic valence band structures of (a) PbTe^{20–22} and (b) SnTe^{17–19} featuring two valence bands separated by an energy difference ΔE at room temperature. (c) Theoretical room-temperature Pisarenko plots for SnTe¹⁰ and PbTe.²³ (d) A comparison of temperature-dependent lattice thermal conductivity for SnTe in this study and PbTe.²⁴

1) with unexpected low lattice thermal conductivity which can be rationally explained by the strong point defect scattering between the filler F in fully filled FCo_4Sb_{12} and the structural vacancy \square in unfilled $\square Co_4Sb_{12}$.^{35,36} Similar results have also been discovered recently in InSb–In₂Te₃ and GeTe–In₂Te₃ systems.^{37,38} It was found that the lattice thermal conductivities of InSb and GeTe are remarkably reduced when alloyed with the proper amount of In₂Te₃ that has an inherent vacancy at the indium sublattice site (one-third of its cationic sites are vacant). This great reduction of lattice thermal conductivity is attributed to the significant vacancy phonon scattering induced by guesting vacancies.^{37,38}

Here in this study, we extend such an approach to the SnTe system. We unravel the coexistence of two beneficial effects by In₂Te₃ alloying with SnTe: (1) a significant decrease of lattice thermal conductivity due to the strong vacancy phonon scattering between the host Sn atoms of SnTe and the guest structural vacancies of In₂Te₃, and an additional interfacial scattering by In-rich nanostructures; (2) a considerable enhancement of Seebeck coefficient because of the resonant levels inside the valence bands of SnTe introduced by indium. As a consequence, the thermoelectric figure of merit ZT of SnTe is largely increased by In₂Te₃ alloying, with the maximum value reaching ~ 0.9 around 923 K which is 50% improvement over the pristine SnTe. Further carrier concentration engineering was made through iodine substitution for Te, leading to a peak $ZT > 1.1$ at ~ 923 K. Together with its high average ZT of ~ 0.67 in the temperature range of 300–923 K and nontoxic constitute elements, In₂Te₃-alloyed SnTe holds great promise as a robust material for high-temperature thermoelectric power generation.

2. EXPERIMENTAL SECTION

2.1. Samples Synthesis. **2.1.1. Weighing.** High-purity (>99.99%) single elements Sn, In, Te, and I₂ were weighed according to the

nominal compositions of (SnTe)_{3–3x}(In₂Te₃)_x ($x = 0, 0.02, 0.04, 0.06, 0.08$, and 0.10 , in mole ratio) and (SnTe_{1–y}I_y)_{2.88}(In₂Te_{3–3y}I_{3y})_{0.04} ($y = 0, 0.2\%, 0.4\%, 0.6\%, 0.8\%$, and 1% , in mole ratio) and then put inside 13 mm diameter fused quartz tubes. The tubes were then evacuated to a residual pressure of $\sim 10^{-4}$ Torr and flame-sealed. With a pumping vacuum for I-containing samples, the tube was immersed in liquid nitrogen so as to reduce the evaporation of iodine. For a typical experiment the following amounts were used: Sn (3.7268 g, 31.39 mmol), In (0.1001 g, 0.872 mmol), Te (4.1478 g, 32.51 mmol), and I₂ (0.0253 g, 0.098 mmol) were used to prepare 8 g of (SnTe_{0.994}I_{0.006})_{2.88}(In₂Te_{2.982}I_{0.018})_{0.04}.

2.1.2. Melting. The samples in the loaded tubes were melted in computer-controlled furnaces. The samples were slowly heated to 1273 K in 10 h, soaked at this temperature for 8 h, then slowly cooled to 873 K in 4 h, dwelled at this temperature for another 24 h, and subsequently cooled to room temperature by switching off the furnace power. The tubes were periodically shaken during the melting process to promote complete reaction among elements and ensure the homogeneity of the compositions.

2.1.3. Densification. The resultant ingots were crushed into fine powders using a mechanic motor and then densified by spark plasma sintering (SPS) method (SPS-211LX, Fuji Electronic Industrial Co., Ltd.) at 773 K for 5 min in a 12.7 mm diameter graphite die under axial compressive stress of 40 MPa in vacuum. Highly dense (6.1–6.3 g/cm³, >97% of theoretical density, Table S1 of the Supporting Information) disk-shaped pellets with dimensions of 12.7 mm diameter and 8 mm thickness were obtained.

2.2. X-ray Diffraction and Differential Thermal Analysis. Samples pulverized with an agate mortar were used for powder X-ray diffraction (PXRD). The powder diffraction patterns were obtained with Cu $K\alpha$ ($\lambda = 1.5418 \text{ \AA}$) radiation in a reflection geometry on an Inel diffractometer operating at 40 kV and 20 mA and equipped with a position-sensitive detector, in a way of real-time data acquisition via the 4096-channel CPS120 detector and a step size of $2\theta = 0.029^\circ$. Differential thermal analysis (DTA) was performed with a computer-controlled Shimadzu DTA-50 thermal analyzer. Freshly ground powder (~ 30 mg total mass) was sealed in a fused quartz ampule under vacuum. An ampule containing α -Al₂O₃ of equal mass was sealed and placed on the reference side of the detector. The sample

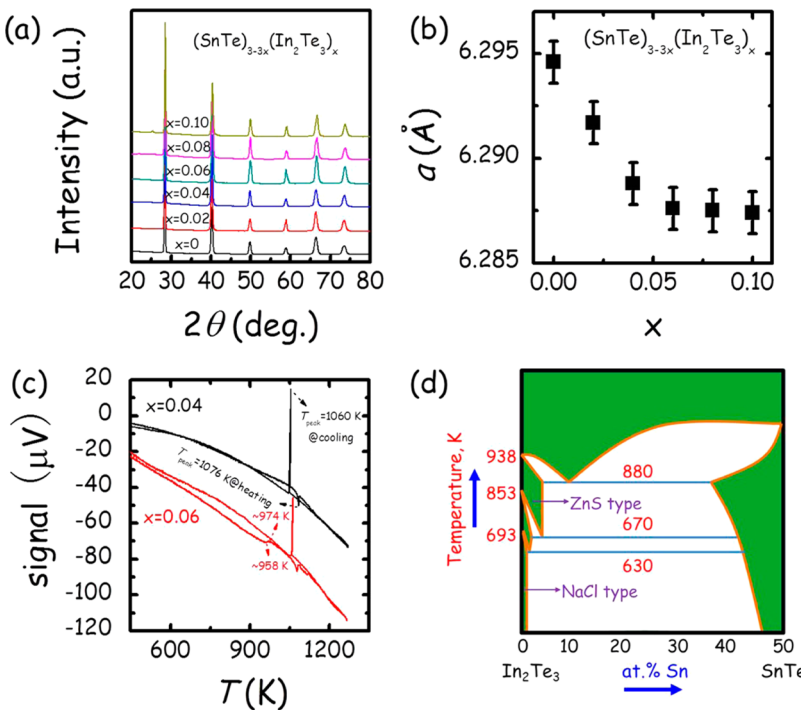


Figure 2. (a) PXRD and (b) lattice parameter of $(\text{SnTe})_{3-3x}(\text{In}_2\text{Te}_3)_x$. (c) DTA curves for two selective samples ($x = 0.04$ and 0.06). (d) A representative SnTe–In₂Te₃ pseudobinary phase diagram.⁴²

and reference were heated to 1273 K and then cooled to 323 K at a rate of 5 K/min.

2.3. Physical Characterization. **2.3.1. Electrical Properties.** The obtained SPS processed pellets were cut into bars with dimensions $\sim 12 \times 3 \times 3 \text{ mm}^3$ for simultaneous measurement of the Seebeck coefficient and electrical conductivity using an Ulvac Riko ZEM-3 instrument under a low-pressure helium atmosphere from room temperature to 923 K. Samples were spray-coated with boron nitride spray to minimize outgassing except where needed for electrical contact with the thermocouples, heater, and voltage probes. The uncertainties of the Seebeck coefficient and electrical conductivity measurements are $\sim 5\%$ and 10%, respectively.³⁹

2.3.2. Thermal Conductivity. Highly dense SPS-processed pellets were cut and polished into a squared shape of $\sim 6 \times 6 \times 2 \text{ mm}^3$ for thermal diffusivity measurements. The samples were coated with a thin layer of graphite to minimize errors from the emissivity of the material. The thermal conductivity was calculated from $\kappa = DC_p d$, where the thermal diffusivity coefficient (D) was measured using the laser flash diffusivity method in a Netzsch LFA457, the specific heat capacity (C_p) of SnTe^{6,7} was adopted for all the samples investigated in this study, and the density (d) was determined using the dimensions and mass of the sample. The thermal diffusivity data were analyzed using a Cowan model with pulse correction. The uncertainty of the thermal conductivity is estimated to be within 16%, considering all the uncertainties from D ($\sim 5\%$), C_p ($\sim 15\%$), and d .³⁹ The thermal diffusion data for all samples can be found in Figure S1. The combined uncertainty for all measurements involved in the calculation of ZT is around 20%. Unless otherwise noted, all the properties described in this study were measured perpendicular to the sintering pressure direction, although no apparent directional anisotropy effects were observed in the charge-transport properties. The influence of point defect scattering on the lattice thermal conductivity was performed using the equations given by Wang et al.³² The parameters for the elastic properties were calculated using a Grüneisen parameter of $\gamma = 2.1$, average speed of sound of 1640 m/s, and a Poisson ratio of 0.244.^{40,41}

2.3.3. Hall Measurements. The room-temperature Hall coefficients were measured on a home-built system in magnetic fields ranging from 0 to 1.25 T, utilizing simple four-contact Hall-bar geometry, in both

negative and positive polarity to eliminate Joule resistive errors. The effective carrier concentration (N_p) was estimated using the relationship $N_p = 1/eR_H$, where e is the elemental charge and R_H is the Hall coefficient. The Hall mobility (μ_H) was calculated using the relationship $\mu_H = \sigma R_H$ with σ being the electrical conductivity obtained from ZEM-3 instrument.

2.4. Transmission Electron Microscopy. (Scanning) Transmission electron microscopy (S/TEM) and STEM energy dispersive spectroscopy (STEM EDS) were conducted by a JEOL 2100F microscope operated at 200 keV. TEM sample was prepared by conventional dimpling and followed by ion milling with liquid N₂ to minimize the ion damage.

3. RESULTS AND DISCUSSION

3.1. Solubility of In₂Te₃ in SnTe. Figure 2a shows the room-temperature PXRD patterns of $(\text{SnTe})_{3-3x}(\text{In}_2\text{Te}_3)_x$ which are practically single-phase compounds that can be indexed to the rock-salt SnTe structure with no second phase being observed within the instrument detection limits. As shown in Figure 2b, the calculated lattice parameter (a) decreases gradually with increasing x until 0.06 and beyond that shows negligible change. This suggests a solubility limit of < 6 mol % for In₂Te₃ in SnTe, which is consistent with a previous study.⁴²

In₂Te₃ has a ZnS-type crystal structure with one-third of its cationic sites vacant. At high temperature, In₂Te₃ crystallizes in β -phase where In atoms and cationic vacancies are randomly distributed, leading to a face-centered cubic cell (space group $F\bar{4}3m$).⁴³ At low temperature, there exists two distinct ordered phases: α -I and α -II. α -I features a one-dimensional long-period superlattice with a tetragonal unit cell while α -II is a superstructure of the β -phase with a high density of stacking faults. α -I and α -II are actually dispersed in each other and cannot be differentiated by XRD.⁴³ Thermal analysis, however, can provide some useful information beyond PXRD. Figure 2c shows the differential thermal analysis (DTA) results for two

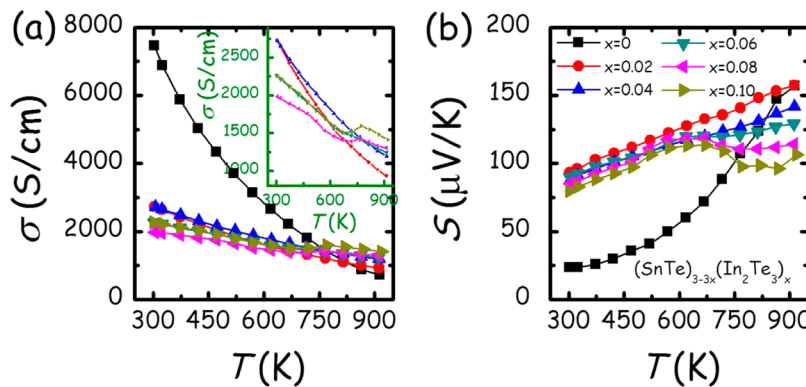


Figure 3. (a) Electrical conductivity and (b) Seebeck coefficient as a function of temperature for $(\text{SnTe})_{3-3x}(\text{In}_2\text{Te}_3)_x$. Inset of (a): temperature-dependent electrical conductivities for $(\text{SnTe})_{3-3x}(\text{In}_2\text{Te}_3)_x$ ($x = 0.02\text{--}0.10$) showing abnormal changes after 650 K for $x \geq 0.06$ samples.

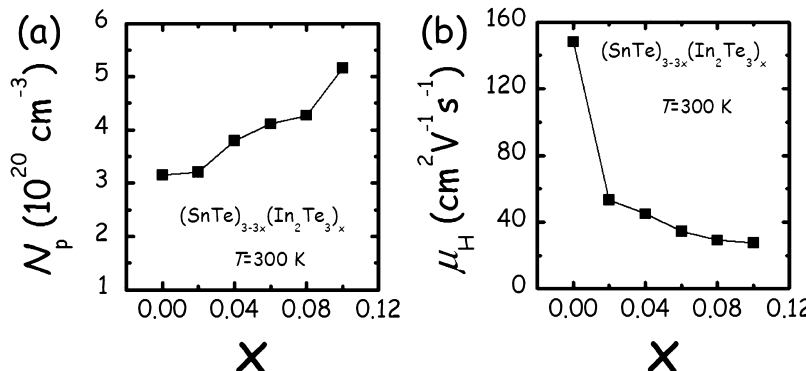


Figure 4. Room-temperature (a): Hall carrier concentration N_p and (b) Hall mobility μ_H as a function of doping amount x for $(\text{SnTe})_{3-3x}(\text{In}_2\text{Te}_3)_x$. The lines are guide to eyes.

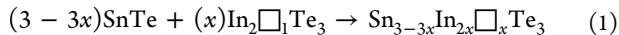
selective samples with $x = 0.04$ and 0.06 , corresponding to the compositions around the solubility limit. For the $x = 0.04$ sample, two well-defined peaks located around 1076 and 1060 K can be observed in the heating and cooling cycles, which respectively correspond to the melting and recrystallization behavior of SnTe (see the representative In_2Te_3 –SnTe pseudobinary phase diagram⁴¹ shown in Figure 2d). However, for the $x = 0.06$ samples, besides the two similar peaks, an extra hump starting around 958 K and peaking at ~974 K is recorded in the DTA curves. Thomassen et al.⁴⁴ found a similar thermal feature around 950 K in the DTA plot for In_2Te_3 , which was attributed to a combination of $\alpha\text{-In}_2\text{Te}_3/\beta\text{-In}_2\text{Te}_3$ phase transformation and the In_4Te_7 (or In_3Te_5) peritectic. Thus, DTA provides conclusive evidence of the presence of an In_2Te_3 impurity phase in the $x = 0.06$ sample, which agrees with the PXRD analysis. However, it cannot exclude the presence of any In_2Te_3 second phase in the $x = 0.04$ sample (microscopic study on $x = 0.04$ sample shown in Figure 9 clearly suggests a phase-separated system). The absence of any In_2Te_3 -related thermal effects in the DTA curve of the $x = 0.04$ sample can be ascribed to many reasons, for example, the size effects and the heating rate which can affect or even mask the phase transitions.

3.2. Resonant Levels Associated with Indium. Figure 3a,b display the temperature-dependent electrical conductivity σ and Seebeck coefficient S respectively for $(\text{SnTe})_{3-3x}(\text{In}_2\text{Te}_3)_x$. As shown in Figure 3a, σ shows negative slope as temperature rises for all samples, indicating a metallic conduction behavior. With increasing In_2Te_3 content, the room-temperature conductivity of $(\text{SnTe})_{3-3x}(\text{In}_2\text{Te}_3)_x$ decreases, which can be attributed to the decrease of hole

mobilities as seen in Figure 4b. However, the electrical conductivity of the In-containing samples has much weaker temperature dependence, due to a reduced phonon scattering which results in higher values at $T > 800 \text{ K}$ when compared with pristine SnTe. For samples with higher In_2Te_3 content ($x \geq 0.06$), the electrical conductivity shows a sudden increase in the temperature range of 650–750 K and afterward decreases almost linearly with increasing temperature; see the inset of Figure 3a. Correspondingly, one can see a bump in the S – T plot between 500 and 700 K (Figure 3b). This abnormal change in electrical conductivity and Seebeck coefficient for the high In_2Te_3 -containing samples is still unclear but might be related to the presence of the In_2Te_3 impurity phase with complex phase transitions (Figure 2d). This can also support the apparent <6% solubility limit of In_2Te_3 in SnTe that was demonstrated by PXRD above.

Pristine SnTe has a very low Seebeck coefficient of $\sim 23 \mu\text{V}/\text{K}$ at room temperature which is consistent with its high hole density of $\sim 3.2 \times 10^{20} \text{ cm}^{-3}$ (Figure 4a) originating from the inherent Sn vacancies.^{45,46} The introduction of In_2Te_3 largely enhances the Seebeck coefficient of SnTe, especially in the low-temperature range. For example, the room-temperature Seebeck coefficient of $x = 0.02$ sample is $\sim 93 \mu\text{V}/\text{K}$, almost 4 times that of pure SnTe, despite its higher hole concentration (Figure 4a). This unique behavior is believed to arise from the resonant levels associated with indium^{10,26} which we will discuss below. However, when more In_2Te_3 is added, the Seebeck coefficient of $(\text{SnTe})_{3-3x}(\text{In}_2\text{Te}_3)_x$ decreases gradually but is still much higher than that of pristine SnTe.

To understand the variation of electrical properties of $(\text{SnTe})_{3-3x}(\text{In}_2\text{Te}_3)_x$ room-temperature Hall measurements were carried out and the derived Hall concentrations N_p and mobilities μ_H as a function of In_2Te_3 content (x) can be found in parts (a) and (b), respectively, of Figure 4. It is found that N_p increases while μ_H decreases with increasing x . The increase of N_p upon In_2Te_3 alloying can be understood using the formula



where \square denotes a vacancy. Equation 1 suggests that when x mol of In_2Te_3 are added to $(3 - x)$ mol of SnTe, there will additionally generate x mole vacancies at the cationic sites (also note that experimentally, the net effect of In doping, including the extra vacancies it induces, is to act as a weak acceptor^{6,10}), contributing to the observed increase of hole concentrations (Figure 4a) and decrease of Seebeck coefficient when $x > 0.04$ (Figure 3b). In a single band picture an increase in carrier concentration and a concurrent increase of the Seebeck coefficient would be counterintuitive; however, as seen in Figure 1c, at higher carrier concentrations the second band at Σ starts to influence the Seebeck coefficient. The decline of μ_H with increasing In_2Te_3 is likely to result from higher scattering rates between carriers when more holes are produced, stronger scattering by more lattice vacancies, interfacial scattering by In-rich nanoprecipitates (Figure 9), and higher hole density of states mass by In-associated resonant levels^{10,26} inside the valence bands which we will discuss in detail below.

Figure 5a plots the room-temperature mobilities μ_H as a function of hole concentrations N_p for $(\text{SnTe})_{3-3x}(\text{In}_2\text{Te}_3)_x$ in this study as well as some other p-type doped SnTe.^{5,6,10,19} The data, including those for nondoped SnTe, and Cu- and Bi-doped SnTe, can be well presented by the straight line on a $\log(\mu_H)$ - $\log(N_p)$ plot. However, the data for the In-containing SnTe ($(\text{Sn}_{1-x}\text{In}_x\text{Te})^{10}$ and $(\text{SnTe})_{3-3x}(\text{In}_2\text{Te}_3)_x$ in this study) lie far below this straight line, suggesting the existence of other scattering mechanisms being responsible for the lower μ_H .

Figure 5b compares the present room-temperature Seebeck coefficient versus hole density data of $(\text{SnTe})_{3-3x}(\text{In}_2\text{Te}_3)_x$ samples with previously reported experimental data on In-, Bi-,^{47,48} and undoped SnTe.^{19,50} The solid line shown in Figure 5b is a theoretical Pisarenko plot calculated on the basis of a two-valence-band model with a light hole band effective mass of $0.168 m_e$ (m_e is the free electron mass), a heavy hole band effective mass of $1.92 m_e$, and an energy difference between the two hole bands of 0.35 eV.¹⁰ Clearly, the data of Bi- and nondoped SnTe agree very well with the Pisarenko plot, demonstrating the validity of the band model and the pure dopant nature of bismuth atoms and tin vacancies (the difference in N_p among various nondoped SnTe is caused by different Sn vacancies^{45,46,49}). However, those In-containing SnTe samples display much higher Seebeck coefficient than predicted by the Pisarenko plot, due to the effect of resonant levels associated with indium atoms.^{6,10,26} The resonant levels are known for their ability to sharply increase the density of states and thus the Seebeck coefficient at a proper Fermi level. This, however, works only near room temperature and below and also leads to an apparent loss of carrier mobility, as we see in Figure 4b.

Figure 6 represents the temperature-dependent power factors for $(\text{SnTe})_{3-3x}(\text{In}_2\text{Te}_3)_x$. It can be seen that the alloying of In_2Te_3 in SnTe significantly increases the power factor over a very broad temperature range because of the largely improved Seebeck coefficient. The sample with the smallest In_2Te_3

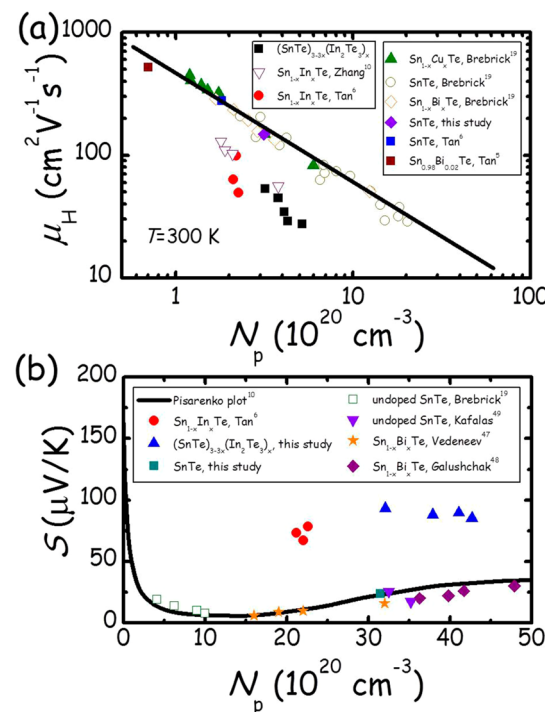


Figure 5. (a) Room-temperature carrier mobilities μ_H as a function of hole concentrations N_p for $(\text{SnTe})_{3-3x}(\text{In}_2\text{Te}_3)_x$ in this study as well as some other p-type doped SnTe from available literature.^{5,6,10,19} The solid line is guide to eyes showing a linear relationship between $\log(\mu_H)$ and $\log(N_p)$. (b) Room-temperature Seebeck coefficient as a function of hole concentrations for $(\text{SnTe})_{3-3x}(\text{In}_2\text{Te}_3)_x$ in this study. The data reported on In-, Bi-,^{47,48} and nondoped SnTe^{19,49} are also included for comparison. The solid line is theoretical Pisarenko plot for SnTe assuming a two valence band model.¹⁰

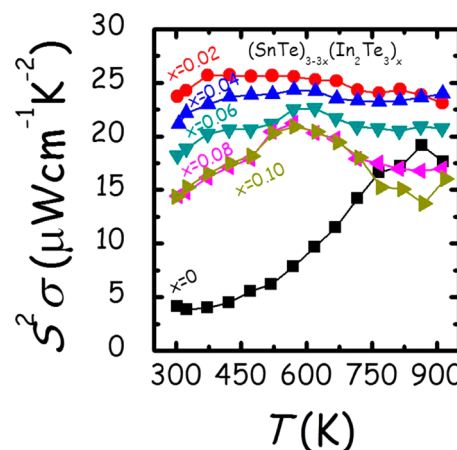


Figure 6. Temperature-dependent power factors for $(\text{SnTe})_{3-3x}(\text{In}_2\text{Te}_3)_x$.

content ($x = 0.02$) possesses the highest power factors. Specifically, the room-temperature power factor for $x = 0.02$ sample is $\sim 23.7 \mu\text{W cm}^{-1} \text{K}^{-2}$, which is nearly 6 times that of pristine SnTe ($\sim 4.1 \mu\text{W cm}^{-1} \text{K}^{-2}$). More importantly, this high power factor is almost temperature-independent, and at high temperature the value is still higher than $23 \mu\text{W cm}^{-1} \text{K}^{-2}$. When the In_2Te_3 content is further increased from 0.02 to 0.10, the power factor of $(\text{SnTe})_{3-3x}(\text{In}_2\text{Te}_3)_x$ slightly decreases due to the simultaneous decrease of electrical conductivity and Seebeck coefficient, but is still much superior to that of pure

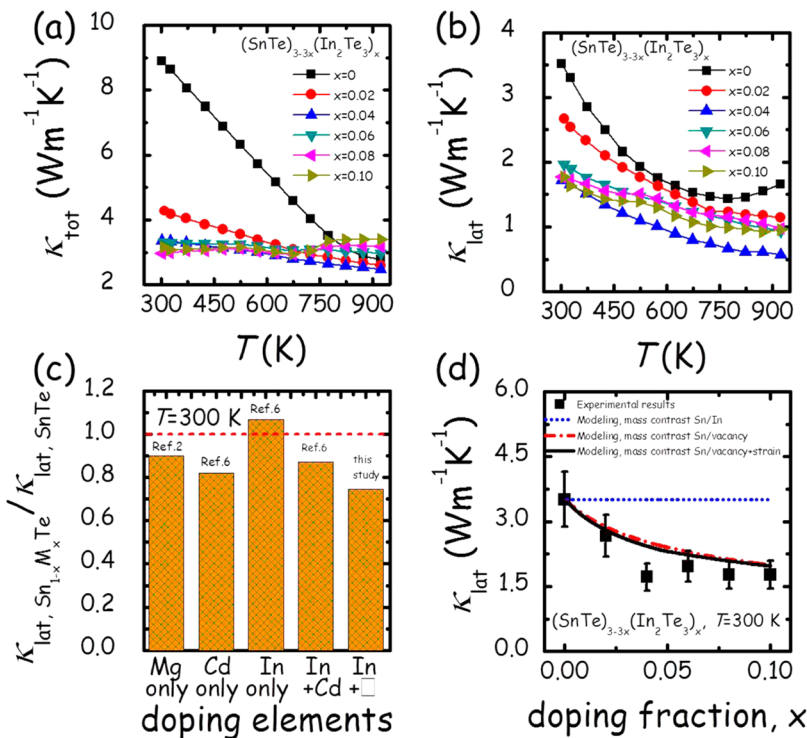


Figure 7. (a) Total and (b) lattice thermal conductivities as a function of temperature for $(\text{SnTe})_{3-3x}(\text{In}_2\text{Te}_3)_x$. (c) A comparison of room-temperature lattice thermal conductivity ratio of doped SnTe to undoped SnTe among Mg singly doped,² Cd singly doped,⁶ In singly doped,⁶ In and Cd codoped,⁶ and In and vacancies codoped SnTe with a similar total doping concentration of ~ 2 mol %. (d) Room-temperature lattice thermal conductivity as a function of doping fraction x for $(\text{SnTe})_{3-3x}(\text{In}_2\text{Te}_3)_x$. The blue dotted line, red dash dotted line, and black solid line represent the fitted lattice thermal conductivities considering the mass contrast between Sn and In, mass contrast between Sn and vacancy, and mass plus strain contrast in total, respectively.

SnTe. The high power factor obtained in $(\text{SnTe})_{3-3x}(\text{In}_2\text{Te}_3)_x$ by In-introduced resonant levels is beneficial to achieve a large ZT , if the thermal conductivity can be lowered.

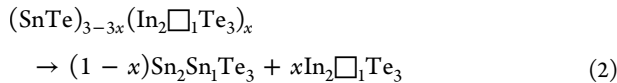
3.3. Strong Vacancy Phonon Scattering. Figure 7a shows the total thermal conductivity (κ_{tot}) of $(\text{SnTe})_{3-3x}(\text{In}_2\text{Te}_3)_x$ as a function of temperature. For the samples with $x \leq 0.04$, κ_{tot} decreases monotonously with increasing temperature. However, for the samples with x being larger than 0.04, κ_{tot} first decreases as temperature rises but starts to increase in the vicinity of 700 K, similar to the trend observed in the electrical conductivity shown in Figure 3a. This abnormal change in κ_{tot} is likely a cause of phase transition associated with In_2Te_3 second phase in these samples. Pristine SnTe in this study features a very high thermal conductivity with the room-temperature value as large as $9 \text{ W m}^{-1} \text{ K}^{-1}$, which is in good agreement with previous studies.^{2,6} A very small amount ($x = 0.02$) of In_2Te_3 alloying in SnTe leads to a dramatic decrease of κ_{tot} to $\sim 4.2 \text{ W m}^{-1} \text{ K}^{-1}$ at room temperature which is only half of that of pristine SnTe. κ_{tot} of SnTe is further decreased with more In_2Te_3 alloying but the magnitude becomes smaller. The significant decrease of κ_{tot} by the introduction of In_2Te_3 in SnTe is partly due to the lessened electrical thermal conductivity (κ_{car} , as a result of decreased electrical conductivity, Figure 3a) and is partly because of the suppression of lattice thermal conductivity (κ_{lat}) which we will show below in Figure 7b.

κ_{lat} can be calculated by subtracting κ_{car} from κ_{tot} while κ_{car} can be estimated using Wiedemann–Franz law, $\kappa_{\text{car}} = L\sigma T$ (L is Lorenz number which can be extracted by fitting the Seebeck coefficient to the reduced chemical potential^{50–53} (Figure S2), σ is the measured electrical conductivity, and T is the

temperature), and the results are shown in Figure 7b. SnTe has the highest lattice thermal conductivity among all the $(\text{SnTe})_{3-3x}(\text{In}_2\text{Te}_3)_x$ samples ranging between 1.4 and $3.5 \text{ W m}^{-1} \text{ K}^{-1}$. There is a clear upturn in the $\kappa_{\text{lat}}-T$ plot for SnTe occurring around 773 K, most likely due to the bipolar diffusion in such a narrow band gap ($\sim 0.1 \text{ eV}$ at 300 K ^{54–56}) semiconductor. κ_{lat} is significantly reduced over the entire measuring temperature range by alloying In_2Te_3 with SnTe, though it becomes saturated when $x > 0.04$. It should be also noted that bipolar diffusion is entirely missing in the In_2Te_3 -containing samples which could be attributed to two factors:⁵⁷ (1) the increase of hole concentration with increasing In_2Te_3 content (Figure 4a); (2) the increase of band gap ($\sim 1.0 \text{ eV}$ at 300 K ⁵⁸) is involved. As it is challenging to directly obtain the band gaps of $(\text{SnTe})_{3-3x}(\text{In}_2\text{Te}_3)_x$ samples by a conventional optical diffuse reflectance technique due to the strong interference from such a high population of free carriers ($> 3 \times 10^{20} \text{ cm}^{-3}$),⁵⁹ it is difficult to assess which factors might be the reason for the suppression of the bipolar effect. The reduction of κ_{lat} at room temperature and the elimination of bipolar diffusion enabled by In_2Te_3 alloying with SnTe yields a pretty low κ_{lat} of $\sim 0.6 \text{ W m}^{-1} \text{ K}^{-1}$ at 923 K for the $x = 0.04$ sample, which is comparable to the value achieved in nanostructured SnTe.^{6,7}

Figure 7c compares the room-temperature lattice thermal conductivity ratio of doped SnTe to pure SnTe for $(\text{SnTe})_{3-3x}(\text{In}_2\text{Te}_3)_x$ in this study with previous reported experimental results on Mg,² Cd,⁶ In,⁶ and Cd/In-doped⁶ SnTe with a similar total doping fraction of ~ 2 mol %. As expected, in comparison to Cd and Mg, In is weakest in reducing κ_{lat} of SnTe because the mass and size differences

between the guest and host atoms is the smallest in the In–Sn case which will usually result in negligible strain contrast. Surprisingly, $(\text{SnTe})_{3-3x}(\text{In}_2\text{Te}_3)_x$ has significantly lower κ_{lat} than $\text{Sn}_{1-x}\text{In}_x\text{Te}$. To assess the origin of this reduction in the lattice thermal conductivity, we modeled the influence of mass and strain contrast using a modified Callaway model.^{29,31,60} Prior to analysis, we need to clarify the existing types of lattice defects in $(\text{SnTe})_{3-3x}(\text{In}_2\text{Te}_3)_x$ as follows:



From eq 2 it is clear that two types of lattice imperfections are present there: two-thirds of them are those between Sn and In atoms while one-third is that between Sn and vacancy \square . With use of the equations and procedures by Wang et al.³² for binary and pseudobinary binary compositions, and accounting for the fractional occupancies, the influence of the mass contrast between Sn and In as well as Sn and vacancy (atomic mass = 0 g/mol) have been calculated (see Figure 7d). The various input parameters can be found in the Experimental Section. While the mass difference between In and Sn has little effect on the lattice thermal conductivity, the influence of vacancy leads to a large reduction in κ_{lat} at room temperature. Since the lattice parameters change with increasing x (Figure 2b), the resulting influence of strain on the lattice thermal conductivity was included into the calculations. The difference between mass contrast Sn/vacancy only and strain-included point defect scattering is small and becomes negligible in the range of constant lattice parameters ($x > 0.06$), showing vacancies are the major influence on the phonon transport. One can see that the experimental data agree reasonably with the theoretical simulation, suggesting the strong vacancy phonon scattering between Sn atoms and lattice vacancies should be largely responsible for the very low lattice thermal conductivity found in $(\text{SnTe})_{3-3x}(\text{In}_2\text{Te}_3)_x$. Observed deviations from the model can be attributed to possible increased boundary scattering via the secondary phase which the point defect model does not account for. Indeed, the lower thermal conductivity at $x = 0.04$ might be due to smaller phase segregations even if the apparent solubility limit has not been reached yet⁶¹ (Figure 9).

Benefiting from the increased power factors and decreased thermal conductivity through In_2Te_3 alloying, the thermoelectric figure of merit ZT of SnTe is markedly enhanced over the entire temperature range (Figure 8). A maximum ZT of ~0.9 at ~923 K is obtained in the $x = 0.04$ sample, which is 50% improvement over the pristine SnTe. We also compare the optimal ZT of the $\text{Sn}_{1-x}\text{In}_x\text{Te}$ system⁶ with our current results in Figure 8. Clearly, $(\text{SnTe})_{3-3x}(\text{In}_2\text{Te}_3)_x$ has superior performance compared to $\text{Sn}_{1-x}\text{In}_x\text{Te}$ because of its lower lattice thermal conductivity mainly resulting from strong vacancy phonon scattering which is however absent in the latter (of course, additional interfacial scattering by In-rich nanoprecipitates cannot be neglected). Nonetheless, one should note that the Seebeck coefficient of $(\text{SnTe})_{3-3x}(\text{In}_2\text{Te}_3)_x$ is low because of the very high hole densities. To pursue an even higher performance, it is necessary to optimize the carrier concentrations of $(\text{SnTe})_{3-3x}(\text{In}_2\text{Te}_3)_x$ to achieve larger Seebeck coefficients, for example, through iodine substitution for tellurium as we will introduce below in Section 3.5.

3.4. Additional Phonon Scattering by Nanostructures.

Microstructural and compositional information on the sample $(\text{SnTe})_{2.88}(\text{In}_2\text{Te}_3)_{0.04}$ have been examined by TEM and STEM

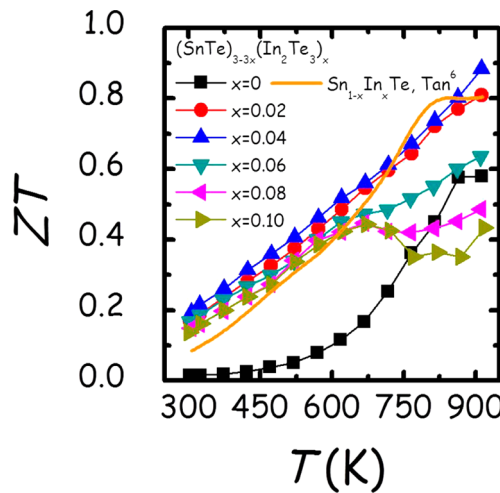


Figure 8. Temperature-dependent ZT values for $(\text{SnTe})_{3-3x}(\text{In}_2\text{Te}_3)_x$. The data for $\text{Sn}_{1-x}\text{In}_x\text{Te}$ ⁶ are also included for comparison.

EDS. Nanoscale precipitates were observed in the low-magnification TEM image, but their density appears notably low, as shown in Figure 9a. The inset selected area electron diffraction (SAED) pattern along [111] shows only one set of spots, indicating small lattice mismatch between the precipitate and the matrix. HRTEM image of one of the precipitates shows Moiré fringes at the interface of the precipitate/matrix, which makes it difficult to determine the coherency of the nanoscale precipitates. The composition investigated by STEM EDS indicates that the precipitates are rich in indium compared to the matrix as shown in Figure S3. The presence of the nanoscale precipitates may contribute to the phonon scattering in addition to the vacancy scattering, which decreases the lattice thermal conductivity even further as shown in Figure 7b. The existence of the nanoprecipitates may also explain the deviation in lattice thermal conductivity between experimental results and the theoretical calculation when $x = 0.04$, as shown in Figure 7d.

3.5. Carrier Concentration Engineering through Iodine Doping. We chose the highest performing $(\text{SnTe})_{2.88}(\text{In}_2\text{Te}_3)_{0.04}$ as the research object for further optimization in the manner of iodine doping up to 1 mol %. The resultant $(\text{SnTe}_{1-y}\text{I})_{2.88}(\text{In}_2\text{Te}_{3-3y}\text{I}_{3y})_{0.04}$ samples are all single-phase compounds within the detection limits of XRD (Figure S4). The temperature-dependent electrical conductivity and Seebeck coefficient of iodine-doped samples are shown in parts (a) and (b), respectively, of Figure 10. As expected, in general, the electrical conductivity decreases while the Seebeck coefficient increases with increasing iodine concentration because iodine as an n-type dopant for Te generates one electron per anion site which reduces the hole carrier densities (Table S2). The highest Seebeck coefficient reaches ~162 $\mu\text{V}/\text{K}$ at ~923 K for the $y = 0.6$ % sample, a 15% improvement over the $y = 0$ sample. It is worth noting that with more iodine being doped, the Seebeck coefficient increases faster as the temperature is rising (Figure 10b). For degenerate semiconductors with parabolic band dispersions, the diffusion part of the Seebeck coefficient (T -linear Seebeck coefficient) can be described as⁶²

$$S = \frac{2\pi^{2/3} k_{\text{B}}^2 m^*}{3^{5/3} e\hbar^2 N_p^{2/3}} \times \left(r + \frac{3}{2} \right) \times T \quad (3)$$

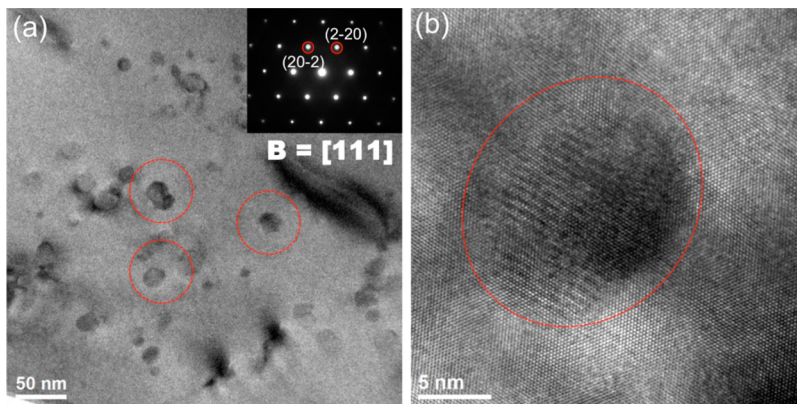


Figure 9. TEM images of the sample $(\text{SnTe})_{2.88}(\text{In}_2\text{Te}_3)_{0.04}$. (a) A low-magnification TEM image of the sample shows nanoscale precipitates, highlighted by the dashed red circles. The corresponding inset SAED pattern indicates the sample is along [111] orientation. (b) The HRTEM image of one of the nanoscale precipitates, highlighted by a dashed red circle.

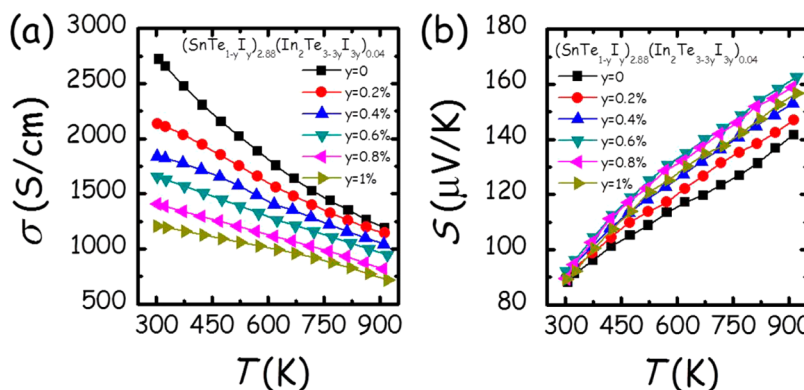


Figure 10. (a) Electrical conductivity and (b) Seebeck coefficient as a function of temperature for $(\text{SnTe}_{1-y}\text{I}_y)_{2.88}(\text{In}_2\text{Te}_{3-3y}\text{I}_{3y})_{0.04}$.

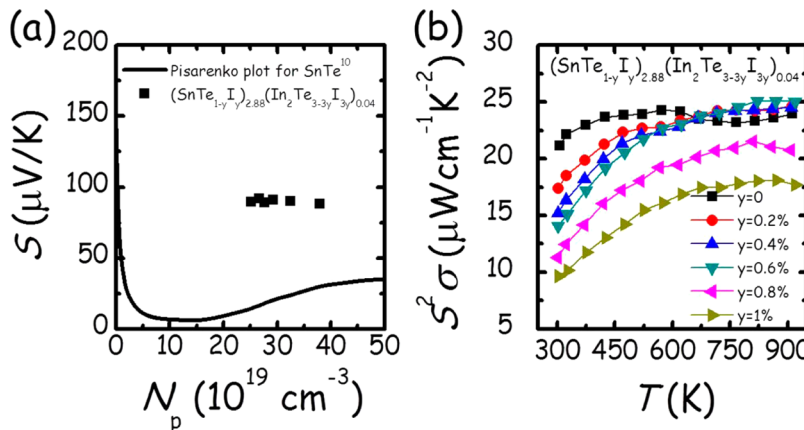


Figure 11. (a) Room-temperature Seebeck coefficient as a function of hole concentrations for $(\text{SnTe}_{1-y}\text{I}_y)_{2.88}(\text{In}_2\text{Te}_{3-3y}\text{I}_{3y})_{0.04}$. The solid line is theoretical Posarenko plot for SnTe assuming a two valence band model.¹⁰ (b) Temperature-dependent power factors for $(\text{SnTe}_{1-y}\text{I}_y)_{2.88}(\text{In}_2\text{Te}_{3-3y}\text{I}_{3y})_{0.04}$.

where k_B is the Boltzmann constant, m^* is the density of states effective mass, e is free electron charge, \hbar is the Plank constant, N_p is the hole concentration, and r is the scattering exponent. From eq 3, it is clear that the larger slope in the $S-T$ plot with increasing iodine content is a consequence of decreased N_p (Table S2).

Figure 11a plots the room-temperature Seebeck coefficient as a function of hole concentration for $(\text{SnTe}_{1-y}\text{I}_y)_{2.88}(\text{In}_2\text{Te}_{3-3y}\text{I}_{3y})_{0.04}$. The solid line is a theoretical Pisarenko plot for SnTe.¹⁰ Apparently, all the samples behave

much higher Seebeck coefficients than predicted by the Pisarenko plot, suggesting the presence of resonant levels^{6,10,26} though iodine is incorporated. The calculated temperature-dependent power factors ($S^2\sigma$) using measured Seebeck coefficient (S) and electrical conductivity (σ) are displayed in Figure 11b. A gradual decrease of power factor with increasing iodine doping fraction is seen in the vicinity of room temperature due to the decline of the electrical conductivity. However, the power factor has no deterioration at high temperature ($T > 650$ K) for the low iodine content ($y \leq 0.6\%$)

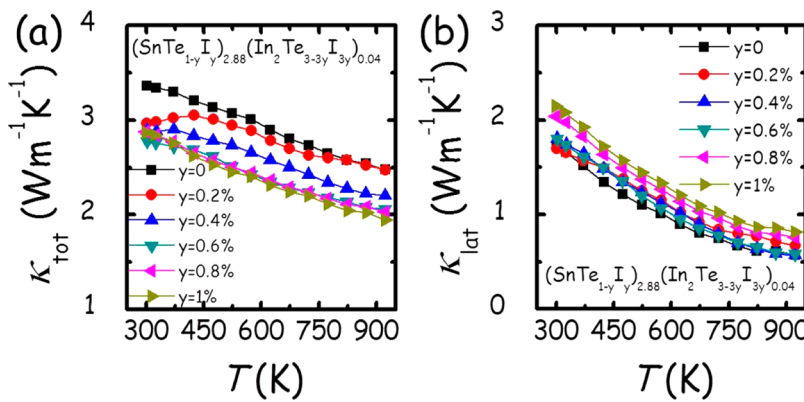


Figure 12. (a) Total and (b) lattice thermal conductivities as a function of temperature for $(\text{SnTe}_{1-y}\text{I}_y)_{2.88}(\text{In}_2\text{Te}_{3-3y}\text{I}_{3y})_{0.04}$.

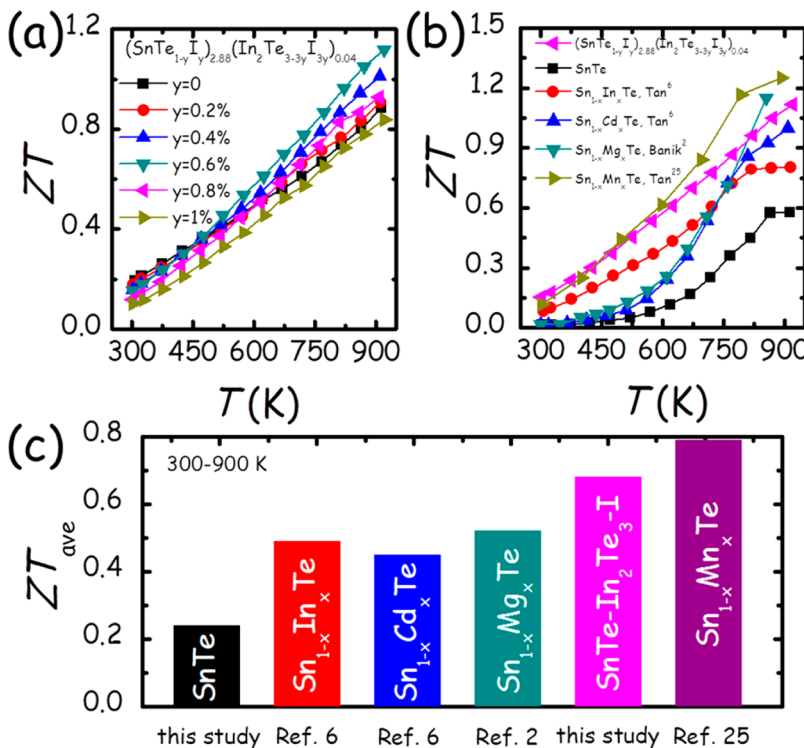


Figure 13. (a) Temperature-dependent ZT values for $(\text{SnTe}_{1-y}\text{I}_y)_{2.88}(\text{In}_2\text{Te}_{3-3y}\text{I}_{3y})_{0.04}$. (b) A comparison of ZT values between $(\text{SnTe}_{1-y}\text{I}_y)_{2.88}(\text{In}_2\text{Te}_{3-3y}\text{I}_{3y})_{0.04}$ in this study and some other p-type doped SnTe.^{2,6,25} (d) 300–900 K average ZTs (ZT_{ave}) calculated for SnTe , $\text{Sn}_{1-x}\text{In}_x\text{Te}$,⁶ $\text{Sn}_{1-x}\text{Cd}_x\text{Te}$,⁶ $\text{Sn}_{1-x}\text{Mg}_x\text{Te}$,² $\text{Sn}_{1-x}\text{Mn}_x\text{Te}$,²⁵ and $(\text{SnTe}_{1-y}\text{I}_y)_{2.88}(\text{In}_2\text{Te}_{3-3y}\text{I}_{3y})_{0.04}$.

samples when compared with the control sample $(\text{SnTe})_{2.88}(\text{In}_2\text{Te}_3)_{0.04}$. This is because the loss of electrical conductivity is compensated by the increase of Seebeck coefficient.

The temperature-relevant total and lattice thermal conductivity for $(\text{SnTe}_{1-y}\text{I}_y)_{2.88}(\text{In}_2\text{Te}_{3-3y}\text{I}_{3y})_{0.04}$ are shown in parts (a) and (b), respectively, of Figure 12. The total thermal conductivity decreases gradually with increasing iodine concentration because of the lessened electronic contribution. The lattice thermal conductivity, however, has less significant composition dependence in comparison with the total thermal conductivity. This is reasonable considering the negligible differences in atomic mass and radii between iodine and tellurium and the very small doping fraction of iodine.

The steadily high power factors along with the decreased thermal conductivities achieved through iodine doping in $(\text{SnTe})_{2.88}(\text{In}_2\text{Te}_3)_{0.04}$ lead to a strong enhancement of ZT

values (Figure 13a). The highest ZT exceeds 1.1 at ~923 K in the $y = 0.6\%$ sample, which is among the best values reported so far for SnTe-based materials^{2,6,25} (Figure 13b). More importantly, its average ZT (ZT_{ave}) between 300 and 900 K is also superior to those of $\text{Sn}_{1-x}\text{Cd}_x\text{Te}$,⁶ $\text{Sn}_{1-x}\text{In}_x\text{Te}$,⁶ and $\text{Sn}_{1-x}\text{Mg}_x\text{Te}$ ² (Figure 13c). In view of its nontoxic constitute element, $(\text{SnTe}_{1-y}\text{I}_y)_{2.88}(\text{In}_2\text{Te}_{3-3y}\text{I}_{3y})_{0.04}$ has great potential as an advanced p-type leg for high-temperature thermoelectric power generation. Note that the ZT_{ave} in this study is lower than that of MnTe heavily alloyed SnTe, where the significantly lowered energy offsets between the two valence bands leads to extremely large Seebeck coefficient at high temperature (~230 $\mu\text{V/K}$ at 900 K).²⁵ In the present study, the indium-related resonant levels are responsible for the enhancement of Seebeck coefficient of SnTe at lower temperatures ($T < 800$ K) and fade at elevated temperature; therefore, a moderate Seebeck coefficient (~160 $\mu\text{V/K}$ at 923 K, Figure 10b) is acquired.

This considerable difference in Seebeck coefficients between In- and heavily Mn-doped SnTe is the main reason for the much larger ZT (thus larger ZT_{ave}) seen in the latter. Future prospects aimed at further increasing the ZT (ZT_{ave}) of SnTe could be combining the merits of In_2Te_3 alloying and Mn doping.

4. CONCLUDING REMARKS

We demonstrated a high thermoelectric performance in p-type SnTe through a combination approach of valence band structure modification (resonant levels) and strong vacancy phonon scattering together with an additional nanostructuring scattering and carrier concentration engineering, realized by In_2Te_3 alloying and iodine doping. Similar to $\text{Sn}_{1-x}\text{In}_x\text{Te}$, the Seebeck coefficient of $(\text{SnTe})_{3-3x}(\text{In}_2\text{Te}_3)_x$ is substantially increased with respect to SnTe, due to In-associated resonant levels inside the valence bands. However, an additionally beneficial effect present in $(\text{SnTe})_{3-3x}(\text{In}_2\text{Te}_3)_x$ is the strong vacancy phonon scattering between tin atoms and lattice vacancies. This enables a considerable suppression of phonon propagation when combined with the scattering from In-rich nanoprecipitates. As a result, a superior performance is observed in $(\text{SnTe})_{3-3x}(\text{In}_2\text{Te}_3)_x$ in relative to $\text{Sn}_{1-x}\text{In}_x\text{Te}$. Iodine substitution for tellurium optimizes the hole density of $(\text{SnTe})_{3-3x}(\text{In}_2\text{Te}_3)_x$, contributing to enhanced Seebeck coefficient and decreased thermal conductivity. Consequently, a high $ZT > 1.1$ at ~ 923 K is achieved in the $(\text{SnTe}_{1-y}\text{I}_y)_{2.88}(\text{In}_2\text{Te}_{3-y}\text{I}_{3y})_{0.04}$ sample with $y = 0.6\%$.

■ ASSOCIATED CONTENT

Supporting Information

Room-temperature densities (Table S1) and hole densities (Table S2) for all the samples investigated in this study; temperature-dependent thermal diffusivities (Figure S1) and Lorenz numbers (Figure S2); STEM EDS results of the sample $(\text{SnTe})_{2.88}(\text{In}_2\text{Te}_3)_{0.04}$ (Figure S3); PXRD of $(\text{SnTe}_{1-y}\text{I}_y)_{2.88}(\text{In}_2\text{Te}_{3-y}\text{I}_{3y})_{0.04}$ ($y = 0\text{--}1\%$) (Figure S4). The Supporting Information is available free of charge on the ACS Publications website at DOI: [10.1021/acs.chemmater.5b03708](https://doi.org/10.1021/acs.chemmater.5b03708).

■ AUTHOR INFORMATION

Corresponding Author

*E-mail: m-kanatzidis@northwestern.edu.

Notes

The authors declare no competing financial interest.

■ ACKNOWLEDGMENTS

This work was supported by the Department of Energy, Office of Science Basic Energy Sciences grant DE-SC0014520. Transmission electron microscopy work was partially performed in the EPIC facility of the NUANCE Center at Northwestern University.

■ REFERENCES

- (1) Banik, A.; Biswas, K. Lead-free thermoelectrics: promising thermoelectric performance in p-type $\text{SnTe}_{1-x}\text{Se}_x$ system. *J. Mater. Chem. A* **2014**, *2*, 9620–9625.
- (2) Banik, A.; Shenoy, U. S.; Anand, S.; Waghmare, U. V.; Biswas, K. Mg Alloying in SnTe Facilitates Valence Band Convergence and Optimizes Thermoelectric Properties. *Chem. Mater.* **2015**, *27*, 581–587.
- (3) Chen, Y.; Nielsen, M. D.; Gao, Y. B.; Zhu, T. J.; Zhao, X.; Heremans, J. P. $\text{SnTe}-\text{AgSbTe}_2$ Thermoelectric Alloys. *Adv. Energy Mater.* **2012**, *2*, 58–62.
- (4) Han, M. K.; Androulakis, J.; Kim, S. J.; Kanatzidis, M. G. Lead-Free Thermoelectrics: High Figure of Merit in p-type $\text{AgSn}_m\text{SbTe}_{m+2}$. *Adv. Energy Mater.* **2012**, *2*, 157–161.
- (5) Tan, G.; Shi, F.; Doak, J. W.; Sun, H.; Zhao, L.-D.; Wang, P.; Uher, C.; Wolverton, C.; Dravid, V. P.; Kanatzidis, M. G. Extraordinary role of Hg in enhancing thermoelectric performance of p-type SnTe. *Energy Environ. Sci.* **2015**, *8*, 267–277.
- (6) Tan, G.; Shi, F.; Hao, S.; Chi, H.; Zhao, L.-D.; Uher, C.; Wolverton, C.; Dravid, V. P.; Kanatzidis, M. G. Codoping in SnTe: Enhancement of Thermoelectric Performance through Synergy of Resonance Levels and Band Convergence. *J. Am. Chem. Soc.* **2015**, *137*, 5100–5112.
- (7) Tan, G.; Zhao, L.-D.; Shi, F.; Doak, J. W.; Lo, S.-H.; Sun, H.; Wolverton, C.; Dravid, V. P.; Uher, C.; Kanatzidis, M. G. High Thermoelectric Performance of p-Type SnTe via a Synergistic Band Engineering and Nanostructuring Approach. *J. Am. Chem. Soc.* **2014**, *136*, 7006–7017.
- (8) Tan, G.; Shi, F.; Sun, H.; Zhao, L.-D.; Uher, C.; Dravid, V. P.; Kanatzidis, M. G. SnTe-AgBiTe₂ as an efficient thermoelectric material with low thermal conductivity. *J. Mater. Chem. A* **2014**, *2*, 20849–20854.
- (9) Xu, E. Z.; Li, Z.; Martinez, J. A.; Sinitsyn, N.; Htoon, H.; Li, N.; Swartzentruber, B.; Hollingsworth, J. A.; Wang, J.; Zhang, S. X. Diameter dependent thermoelectric properties of individual SnTe nanowires. *Nanoscale* **2015**, *7*, 2869–2876.
- (10) Zhang, Q.; Liao, B.; Lan, Y.; Lukas, K.; Liu, W.; Esfarjani, K.; Opeil, C.; Brodo, D.; Chen, G.; Ren, Z. High thermoelectric performance by resonant dopant indium in nanostructured SnTe. *Proc. Natl. Acad. Sci. U. S. A.* **2013**, *110*, 13261–13266.
- (11) Zhou, M.; Gibbs, Z. M.; Wang, H.; Han, Y.; Xin, C.; Li, L.; Snyder, G. J. Optimization of thermoelectric efficiency in SnTe: the case for the light band. *Phys. Chem. Chem. Phys.* **2014**, *16*, 20741–20748.
- (12) Liang, T.; Su, X.; Tan, X.; Zheng, G.; She, X.; Yan, Y.; Tang, X.; Uher, C. Ultra-fast non-equilibrium synthesis and phase segregation in $\text{In}_x\text{Sn}_{1-x}\text{Te}$ thermoelectrics by SHS-PAS processing. *J. Mater. Chem. C* **2015**, *3*, 8550–8558.
- (13) Hsu, K. F.; Loo, S.; Guo, F.; Chen, W.; Dyck, J. S.; Uher, C.; Hogan, T.; Polychroniadis, E.; Kanatzidis, M. G. Cubic $\text{AgPb}_m\text{SbTe}_{2+m}$: bulk thermoelectric materials with high figure of merit. *Science* **2004**, *303*, 818–821.
- (14) Pei, Y.; Shi, X.; LaLonde, A.; Wang, H.; Chen, L.; Snyder, G. J. Convergence of electronic bands for high performance bulk thermoelectrics. *Nature* **2011**, *473*, 66–69.
- (15) Biswas, K.; He, J.; Blum, I. D.; Wu, C.-I.; Hogan, T. P.; Seidman, D. N.; Dravid, V. P.; Kanatzidis, M. G. High-performance bulk thermoelectrics with all-scale hierarchical architectures. *Nature* **2012**, *489*, 414–418.
- (16) Heremans, J. P.; Jovovic, V.; Toberer, E. S.; Saramat, A.; Kurosaki, K.; Charoenphakdee, A.; Yamanaka, S.; Snyder, G. J. Enhancement of thermoelectric efficiency in PbTe by distortion of the electronic density of states. *Science* **2008**, *321*, 554–557.
- (17) Rogers, L. Valence band structure of SnTe. *J. Phys. D: Appl. Phys.* **1968**, *1*, 845–852.
- (18) Santhanam, S.; Chaudhuri, A. Transport properties of SnTe interpreted by means of a two valence band model. *Mater. Res. Bull.* **1981**, *16*, 911–917.
- (19) Brebrick, R. F.; Strauss, A. J. Anomalous Thermoelectric Power as Evidence for Two-Valence Bands in SnTe. *Phys. Rev.* **1963**, *131*, 104–110.
- (20) Sitter, H.; Lischka, K.; Heinrich, H. Structure of the second valence band in PbTe. *Phys. Rev. B* **1977**, *16*, 680–687.
- (21) Allgaier, R. Valence bands in lead telluride. *J. Appl. Phys.* **1961**, *32*, 2185–2189.
- (22) Andreev, A.; Radionov, V. Determination of the band structure of lead telluride from the measurements of the Hall effect at high

- temperatures (Forbidden band structure of PbTe and electrical conductivity and Hall effect measurements at high temperatures). *Sov. Phys. Semicond.* **1967**, *1*, 145–148.
- (23) Airapetyants, S.; Vinogradova, M.; Dubrovskaya, I.; Kolomoets, N.; Rudnik, I. Structure of the valence band of heavily doped lead telluride. *Sov. Phys. Solid State* **1966**, *8*, 1069–1072.
- (24) Pei, Y.-L.; Liu, Y. Electrical and thermal transport properties of Pb-based chalcogenides: PbTe, PbSe, and PbS. *J. Alloys Compd.* **2012**, *S14*, 40–44.
- (25) Tan, G.; Shi, F.; Hao, S.; Chi, H.; Bailey, T. P.; Zhao, L.-D.; Uher, C.; Wolverton, C.; Dravid, V. P.; Kanatzidis, M. G. Valence Band Modification and High Thermoelectric Performance in SnTe Heavily Alloyed with MnTe. *J. Am. Chem. Soc.* **2015**, *137*, 11507–11516.
- (26) Bushmarina, G.; Gruzinov, B.; Drabkin, I.; Lev, E. Y.; Yuneev, V. Characteristics of the effects of In as a dopant in SnTe. *Sov. Phys. Semicond.* **1984**, *18*, 1374–1377.
- (27) Zhang, Q.; Wang, H.; Liu, W.; Wang, H.; Yu, B.; Zhang, Q.; Tian, Z.; Ni, G.; Lee, S.; Esfarjani, K.; Chen, G.; Ren, Z. Enhancement of thermoelectric figure-of-merit by resonant states of aluminium doping in lead selenide. *Energy Environ. Sci.* **2012**, *5*, 5246–5251.
- (28) Abeles, B. Lattice Thermal Conductivity of Disordered Semiconductor Alloys at High Temperatures. *Phys. Rev.* **1963**, *131*, 1906–1911.
- (29) Alekseeva, G.; Efimova, B.; Ostrovskaya, L.; Serebryannikova, O.; Tsypin, M. Thermal conductivity of solid solutions based on lead telluride. *Sov. Phys. Semicond.* **1971**, *4*, 1122–1125.
- (30) Zhou, Z.; Uher, C.; Jewell, A.; Caillat, T. Influence of point-defect scattering on the lattice thermal conductivity of solid solution Co(Sb_{1-x}As_x)₃. *Phys. Rev. B: Condens. Matter Mater. Phys.* **2005**, *71*, 235209.
- (31) Yang, J.; Meisner, G.; Chen, L. Strain field fluctuation effects on lattice thermal conductivity of ZrNiSn-based thermoelectric compounds. *Appl. Phys. Lett.* **2004**, *85*, 1140–1142.
- (32) Wang, H.; Wang, J.; Cao, X.; Snyder, G. J. Thermoelectric alloys between PbSe and PbS with effective thermal conductivity reduction and high figure of merit. *J. Mater. Chem. A* **2014**, *2*, 3169–3174.
- (33) Zeier, W. G.; Pei, Y.; Pomrehn, G.; Day, T.; Heinrich, C. P.; Snyder, G. J.; Tremel, W. Phonon Scattering through a Local Anisotropic Structural Disorder in the Thermoelectric Solid Solution Cu₂Zn_{1-x}Fe_xGeSe₄. *J. Am. Chem. Soc.* **2013**, *135*, 726–732.
- (34) Heinrich, C. P.; Day, T. W.; Zeier, W. G.; Snyder, G. J.; Tremel, W. Effect of Isovalent Substitution on the Thermoelectric Properties of the Cu₂ZnGeSe_{4-x}S_x Series of Solid Solutions. *J. Am. Chem. Soc.* **2014**, *136*, 442–448.
- (35) Meisner, G.; Morelli, D.; Hu, S.; Yang, J.; Uher, C. Structure and lattice thermal conductivity of fractionally filled skutterudites: Solid solutions of fully filled and unfilled end members. *Phys. Rev. Lett.* **1998**, *80*, 3551–3554.
- (36) Nolas, G.; Cohn, J.; Slack, G. Effect of partial void filling on the lattice thermal conductivity of skutterudites. *Phys. Rev. B: Condens. Matter Mater. Phys.* **1998**, *58*, 164–170.
- (37) Pei, Y.; Morelli, D. T. Vacancy phonon scattering in thermoelectric In₂Te₃–InSb solid solutions. *Appl. Phys. Lett.* **2009**, *94*, 122112.
- (38) Sun, H.; Lu, X.; Chi, H.; Morelli, D. T.; Uher, C. Highly efficient (In₂Te₃)_x(GeTe)_{3-3x} thermoelectric materials: a substitute for TAGS. *Phys. Chem. Chem. Phys.* **2014**, *16*, 15570–15575.
- (39) Borup, K. A.; de Boor, J.; Wang, H.; Drymiotis, F.; Gascoin, F.; Shi, X.; Chen, L.; Fedorov, M. I.; Muller, E.; Iversen, B. B.; Snyder, G. J. Measuring thermoelectric transport properties of materials. *Energy Environ. Sci.* **2015**, *8*, 423–435.
- (40) Toher, C.; Plata, J. J.; Levy, O.; de Jong, M.; Asta, M.; Nardelli, M. B.; Curtarolo, S. High-throughput computational screening of thermal conductivity, Debye temperature, and Grüneisen parameter using a quasiharmonic Debye model. *Phys. Rev. B: Condens. Matter Mater. Phys.* **2014**, *90*, 174107.
- (41) Schmidt, R. D.; Case, E. D.; Ni, J. E.; Trejo, R. M.; Lara-Curcio, E.; Korkosz, R. J.; Kanatzidis, M. G. High-temperature elastic moduli of thermoelectric SnTe_{1±x}–ySiC nanoparticulate composites. *J. Mater. Sci.* **2013**, *48*, 8244–8258.
- (42) Babaev, A. N.; Rustamov, P. G.; Gusejnov, V. G. Interaction of tin telluride with gallium and indium sesquitellurides. *Russ. J. Inorg. Chem.* **1985**, *30*, 1802–1804.
- (43) Karakostas, T.; Economou, N. Ordered phases of In₂Te₃. *Phys. Status Solidi A* **1975**, *31*, 89–99.
- (44) Thomassen, L.; Mason, D. R.; Rose, G. D.; Sarace, J. C.; Schmitt, G. A. The Phase Diagram for the Pseudo-binary System CdTe-In₂Te₃. *J. Electrochem. Soc.* **1963**, *110*, 1127–1131.
- (45) Rogacheva, E. I. The problem of doping of non-stoichiometric phases. *J. Phys. Chem. Solids* **2008**, *69*, 259–268.
- (46) Nashchekina, O.; Rogacheva, E.; Popov, V. Nonstoichiometry and thermal expansion of SnTe. *J. Phys. Chem. Solids* **2008**, *69*, 273–277.
- (47) Vedeneev, V.; Krivoruchko, S.; Sabo, E. Tin telluride based thermoelectrical alloys. *Semiconductors* **1998**, *32*, 241–244.
- (48) Galushchak, M.; Freik, D.; Ivanyshyn, I.; Lisak, A.; Pyts, M. Thermoelectric Properties and Defective Subsystem in Doped Telluride of Tin. *J. Thermoelectr.* **2000**, *1*, 42–50.
- (49) Kafalas, J.; Brebrick, R.; Strauss, A. Evidence That SnTe is a Semiconductor. *Appl. Phys. Lett.* **1964**, *4*, 93–94.
- (50) Tan, G.; Liu, W.; Chi, H.; Su, X.; Wang, S.; Yan, Y.; Tang, X.; Wong-Ng, W.; Uher, C. Realization of high thermoelectric performance in p-type unfilled ternary skutterudites FeSb_{2+x}Te_{1-x} via band structure modification and significant point defect scattering. *Acta Mater.* **2013**, *61*, 7693–7704.
- (51) Tan, G.; Wang, S.; Yan, Y.; Li, H.; Tang, X. Enhanced thermoelectric performance in p-type Ca_{0.5}Ce_{0.5}Fe_{4-x}Ni_xSb₁₂ skutterudites by adjusting the carrier concentration. *J. Alloys Compd.* **2012**, *S13*, 328–333.
- (52) May, A. F.; Toberer, E. S.; Saramat, A.; Snyder, G. J. Characterization and analysis of thermoelectric transport in n-type Ba₂Ga_{16-x}Ge_{30+x}. *Phys. Rev. B: Condens. Matter Mater. Phys.* **2009**, *80*, 125205.
- (53) Su, X.; Fu, F.; Yan, Y.; Zheng, G.; Liang, T.; Zhang, Q.; Cheng, X.; Yang, D.; Chi, H.; Tang, X.; Zhang, Q.; Uher, C. Self-propagating high-temperature synthesis for compound thermoelectrics and new criterion for combustion processing. *Nat. Commun.* **2014**, *5*, 4908.
- (54) Dimmock, J.; Melngailis, I.; Strauss, A. Band structure and laser action in Pb_xSn_{1-x}Te. *Phys. Rev. Lett.* **1966**, *16*, 1193–1196.
- (55) Dixon, J.; Bis, R. Band Inversion and the Electrical Properties of Pb_xSn_{1-x}Te. *Phys. Rev.* **1968**, *176*, 942–949.
- (56) Ishida, A.; Tsuchiya, T.; Yamada, T.; Cao, D.; Takaoka, S.; Rahim, M.; Felder, F.; Zogg, H. Electrical and optical properties of SnEuTe and SnSrTe films. *J. Appl. Phys.* **2010**, *107*, 123708.
- (57) Nolas, G. S.; Sharp, J.; Goldsmid, H. J. *Thermoelectrics: Basic Principles and New Materials Developments*; Springer: Berlin, 2001.
- (58) Madelung, O. *Semiconductors: data handbook*; Springer: Berlin, 2004.
- (59) Zemel, J. N.; Jensen, J. D.; Scholar, R. B. Electrical and optical properties of epitaxial films of PbS, PbSe, PbTe, and SnTe. *Phys. Rev.* **1965**, *140*, A330–A342.
- (60) Callaway, J.; von Baeyer, H. C. Effect of point imperfections on lattice thermal conductivity. *Phys. Rev.* **1960**, *120*, 1149–1154.
- (61) Zeier, W. G.; LaLonde, A.; Gibbs, Z. M.; Heinrich, C. P.; Panthöfer, M.; Snyder, G. J.; Tremel, W. Influence of a Nano Phase Segregation on the Thermoelectric Properties of the p-Type Doped Stannite Compound Cu_{2+x}Zn_{1-x}GeSe₄. *J. Am. Chem. Soc.* **2012**, *134*, 7147–7154.
- (62) Ravich, I. U. I.; Efimova, B. A.; Smirnov, I. A. *Semiconducting Lead Chalcogenides*; Plenum Press: New York, 1970.